Sensors and Materials, Vol. 37, No. 2 (2025) 509–518
MYU Tokyo

S & M 3926

Evaluation of Radiation Response Properties of Eu_2O_3-doped Bi_2O_3–ZnO–TeO_2 Glass and Glass Ceramics

Shuntaro Muneta,[1*] Naoki Kawano,[1**] Daisuke Nakauchi,[2] Takumi Kato,[2] Kai Okazaki,[2] Kensei Ichiba,[2] Toshiaki Kunikata,[2] Akihiro Nishikawa,[2] Keiichiro Miyazaki,[2] Fumito Kagaya,[1] Kenji Shinozaki,[3,4] and Takayuki Yanagida[2]

[1]Graduate School of Engineering Science, Akita University, 1-1 Tegata Gakuen-machi, Akita 010-8502, Japan
[2]Graduate School of Science and Technology, Nara Institute of Science and Technology, 8916-5 Takayama-cho, Ikoma, Nara 630-0192, Japan
[3]National Institute of Advanced Industrial Science and Technology (AIST), 1-8-31 Midorigaoka, Ikeda, Osaka 563-8577, Japan
[4]Osaka University, 2-1 Yamadaoka, Suita, Osaka 565-0871, Japan

(Received October 30, 2024; accepted January 8, 2025)

Keywords: scintillator, tellurite glass, glass ceramics, luminescence, Eu^{3+}

We prepared a $1Eu_2O_3$–$13Bi_2O_3$–12ZnO–$74TeO_2$ glass (PG) and its glass ceramics (GC340, GC350, and GC360) and evaluated their luminescence properties for scintillators. GC340, GC350, and GC360 were obtained by heat treatment of PG for 24 h at 340, 350, and 360 °C, respectively. Distinct luminescence peaks derived from the radiative transition between 4f levels of Eu^{3+} appeared in PG, GC340, GC350, and GC360 when excited by X-rays or visible light. The scintillation intensity was enhanced by increasing the heat treatment temperature of PG, whereas the quantum yield in photoluminescence was decreased by heat treatment. The results suggest that the energy transfer efficiency in the host material might be increased by heat treatment.

1. Introduction

Scintillators are phosphor materials that immediately convert the absorbed ionizing radiation into many low-energy photons.(1) These photons are usually changed into electrical signals by a photodetector to obtain information on ionizing radiation. A radiation detector that is composed of a scintillator and a photodetector is widely employed in a wide variety of applications, including medical devices, security systems, and spectroscopy systems at a synchrotron facility.(2) Conventionally, single crystals (e.g., NaI:Tl, CsI:Tl, and $Bi_4Ge_3O_{12}$) have been used as scintillators because of their high luminescence intensity.(1) However, existing single-crystal scintillators could have some industrial disadvantages (e.g., high fabrication cost and difficulty in producing a large-volume material).(3) In addition, glass is also a well-known material for scintillators. Glass scintillators have some industrial merits such as their reasonable cost, high productivity, and flexible glass composition.(4,5) So far, the silicate glass GS-20 ($0.7Ce_2O_3$–$31.5Li_2O$–$9.8Al_2O_3$–5.5MgO–$52.5SiO_2$) for detecting thermal neutrons has been developed.(6)

*Corresponding author: e-mail: m8023219@s.akita-u.ac.jp
**Corresponding author: e-mail: n-kawano@gipc.akita-u.ac.jp
https://doi.org/10.18494/SAM5441

ISSN 0914-4935
https://myukk.org/

Nevertheless, there are only a few commercial glass scintillators since glasses often show a low scintillation intensity owing to the low energy transfer efficiency of charged carriers in a glass host.[7]

Recently, glass ceramics have attracted research attention as a new scintillator material. Glass ceramics are a type of composite that has a crystalline phase within an amorphous glassy phase, and glass ceramics can be produced by the heat treatment of a precursor glass under controlled conditions.[8] In several glass systems (e.g., $BaO–TiO_2–SiO_2$, $Gd_2O_3–WO_3–SiO_2–Tb_4O_7$, and $SiO_2–Al_2O_3–Na_2O–BaO–BaF_2–TbF_3$), the increase in scintillation intensity through the precipitation of a crystalline phase has been reported.[9–11] For instance, the integrated scintillation intensity of a Eu^{3+}-doped $GeO_2–Al_2O_3–Na_2O–LiF–LaF_3$ glass ceramic with a fluoride crystalline phase was twice that of its glass, which was attributable to the precipitation of Eu^{3+} in the fluoride crystalline phase that provides a low-phonon-energy environment.[12]

In this study, tellurite glasses were selected as glass hosts. Tellurite glasses have the following interesting features compared with common glasses such as borate glasses. They have in general low phonon energy; therefore, they might exhibit a high luminescence intensity because of the suppression of nonradiative loss. Moreover, owing to their high effective atomic number, they are expected to show high detection efficiency of high-energy electromagnetic fields (e.g., X-rays and γ-rays).[13] To date, several research studies have been conducted on the scintillation properties of tellurite glasses with various luminescence centers, including $Nd_2O_3–BaO–Al_2O_3–TeO_2$, $Pr_2O_3–SrO–Al_2O_3–TeO_2$, and $Er_2O_3–BaO–Nb_2O_5–TeO_2$.[14–16] In particular, tellurite glasses doped with Eu^{3+} tend to exhibit a high quantum yield (*QY*) and a high luminescence intensity under X-ray irradiation, and $5Eu_2O_3–5Al_2O_3–5SrO–85TeO_2$ glass showed efficient photoluminescence (PL) with a *QY* of approximately 80% owing to the radiative transitions between 4f levels in Eu^{3+}, and the integrated intensity of this glass under X-ray irradiation was approximately 2.3% that of a $Bi_4Ge_3O_{12}$ single crystal.[17]

Furthermore, the scintillation properties of tellurite glass ceramics have been evaluated. In a previous study of a $10Eu_2O_3–10BaO–80TeO_2$ glass, the heat treatment of the tellurite glass at 435 or 455 °C resulted in the generation of a $Eu_2Te_6O_{15}$ crystalline phase, leading to an increase in the luminescence intensity under X-ray irradiation.[18] Furthermore, the scintillation properties of $1Eu_2O_3–3BaO–20Nb_2O_5–76TeO_2$ glass and glass ceramics were evaluated. In this case, the $Nb_2Te_4O_{13}$ crystalline phase was generated after heat treatment at 540 °C, but the scintillation intensity was not improved.[19] As mentioned above, the scintillation properties of a few tellurite glass ceramics have been evaluated, but there is considerable room for investigating their scintillation properties.[18–20] In this study, we synthesized a tellurite glass with the $1Eu_2O_3–13Bi_2O_3–12ZnO–74TeO_2$ composition and its glass ceramics, and evaluated their scintillation properties.

2. Experimental Methods

Eu_2O_3 (Kasei Optonix), Bi_2O_3, ZnO, and TeO_2 (High Purity Chemical Laboratory, Inc.) were prepared as starting materials. These starting materials were mixed after weighing based on the glass composition of $1Eu_2O_3–13Bi_2O_3–12ZnO–74TeO_2$, and the mixture was placed in a

platinum crucible and melted in a furnace for 40 min at 850 °C. The resulting melt was subsequently quenched on a plate at 300 °C to synthesize $1Eu_2O_3$–$13Bi_2O_3$–12ZnO–$74TeO_2$ glass (PG). PG was polished to a thickness of approximately 1.5 mm. Moreover, its glass ceramics (GC340, GC350, and GC360) were synthesized by heating PG at 340, 350, and 360 °C for 24 h, respectively, as shown in Table 1.

Differential thermal analysis (DTA) of PG was performed using a TG-DTA200SA analyzer (Bruker) to determine its glass transition temperature (T_g) and crystallization temperature (T_x). X-ray diffraction (XRD) patterns were measured using an RINT-2200 V diffractometer (Rigaku) to investigate the crystal structure in PG, GC340, GC350, and GC360. A V760 spectrometer (JASCO) was used for the measurement of in-line transmission spectra. PL spectra were recorded using an RF-6000 fluorescence spectrometer (Shimadzu Corporation). To evaluate *QY*, a C11347 spectrometer (Hamamatsu Photonics) was employed. In addition, the PL decay time profile was recorded using a C16361 spectrometer (Hamamatsu Photonics). Scintillation spectra were recorded using an evaluation system with a DU-420-BU2 spectrometer (Andor) and an optical fiber.[21] In addition, pulse X-ray scintillation decay curves and afterglow profiles were recorded using our setup.[22]

3. Results and Discussion

The images of PG, GC340, GC350, and GC360 are shown in Fig. 1. PG and GC340 were so transparent that the line patterns behind the samples were clearly visible. On the other hand, GC350 and GC360 were translucent. To investigate their transparency, the transmittance spectra of PG, GC340, GC350, and GC360 were recorded (Fig. 2). The transmittances at 650 nm were 74.8% (PG), 69.5% (GC340), 7.3% (GC350), and 27.8% (GC360). The reason for the higher transmittance of GC360 than of GC350 is unclear, and the presence of a crystalline phase should lead to the decrease in transmittance, but the transmittance might have been increased by the

Table 1
Heat treatment conditions and sample codes.

Sample code	Heat treatment condition
PG	–
GC340	340 °C for 24 h
GC350	350 °C for 24 h
GC360	360 °C for 24 h

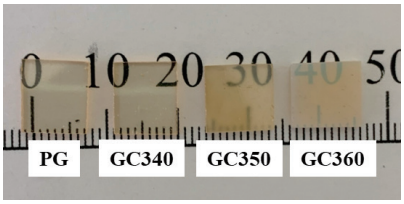

Fig. 1. (Color online) Images of PG, GC340, GC350, and GC360.

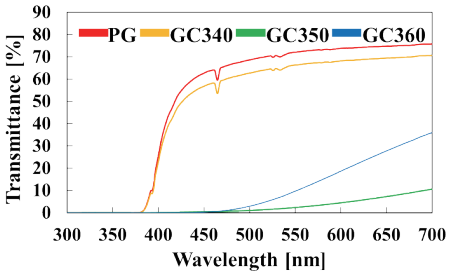

Fig. 2. (Color online) Transmittance spectra of PG, GC340, GC350, and GC360.

heat treatment because of the resulting decrease in the number of light scattering sources such as point defects in the glass phase after the heat treatment. Furthermore, three absorption bands at 465, 526, and 534 nm appeared in PG and GC340, and these bands should originate from the electronic transition between 4f levels in Eu^{3+}.[12,17,23]

The DTA of PG was performed to determine its T_g and T_x (Fig. 3). From the profile, the T_g of PG was determined to be 320.5 °C, indicating the formation of the glass structure in $1Eu_2O_3$–$13Bi_2O_3$–$12ZnO$–$74TeO_2$. Furthermore, a T_x of 389.0 °C was also obtained, suggesting that the thermal stability (ΔT) derived with the formula ($\Delta T = T_x - T_g$) was 68.5 °C.

The XRD patterns of PG, GC340, GC350, and GC360 were measured (Fig. 4). PG showed a broad diffraction peak from 24° to 36°, confirming a typical amorphous structure. In contrast, GC340, GC350, and GC360 showed sharp diffraction peaks that were identified to be the $Bi_{0.864}Te_{0.136}O_{1.568}$ crystalline phase, indicating that the phase was successfully grown inside the glassy phase.[20,24] Furthermore, the diffraction peak intensity increased with the heat treatment temperature of PG. This result suggests that the size of the $Bi_{0.864}Te_{0.136}O_{1.568}$ crystalline phase might increase in the PG host.

The PL spectra of PG, GC340, GC350, and GC360 under 530 nm light are shown in Fig. 5(a). The five peaks are observed at 579 nm ($^5D_0 \rightarrow {}^7F_0$), 590 nm ($^5D_0 \rightarrow {}^7F_1$), 615 nm ($^5D_0 \rightarrow 7F_2$), 654 nm ($^5D_0 \rightarrow {}^7F_3$), and 703 nm ($^5D_0 \rightarrow {}^7F_4$). These emission peaks originated from the transition between 4f levels in Eu^{3+}.[12,13,17] The $^5D_0 \rightarrow {}^7F_2$ transition is identified as a hypersensitive electric dipole transition in Eu^{3+}, and luminescence intensity is affected by the surrounding environment on Eu^{3+}. Furthermore, the $^5D_0 \rightarrow {}^7F_1$ transition is related to the magnetic dipole transition, and the luminescence intensity is almost independent of the surrounding environment. To investigate the surrounding environment on Eu^{3+}, the red/orange (R/O) ratio, which is the ratio of the luminescence intensity at 615 nm ($^5D_0 \rightarrow {}^7F_2$) to 590 nm ($^5D_0 \rightarrow {}^7F_1$), was calculated, and the results are shown in Fig. 5(b). The R/O ratios were found to be 3.12, 3.12, 2.55, and 2.54 for PG, GC340, GC350, and GC360, respectively. The R/O ratio was decreased by the heat treatment of PG. This indicates that the precipitation of the $Bi_{0.864}Te_{0.136}O_{1.568}$ crystalline phase might lead to high symmetry of the surrounding environment on Eu^{3+}.[19,25] In addition, *QY*s were recorded using 530 nm excitation light. The obtained *QY*s of PG, GC340, GC350, and GC360 were 20, 20, 11, and 12%, respectively. The lower *QY*s of GC350 and GC360 should be associated with the generation of the $Bi_{0.864}Te_{0.136}O_{1.568}$ crystalline phase. Owing to the precipitation of the phase, some Eu^{3+} ions might be located at the Bi^{3+} ion sites because of the same ionic valence number (Bi^{3+}, Te^{4+}, O^{2-}), and the higher symmetry of the surrounding environment on Eu^{3+} might lead to the decrease in *QY*s.

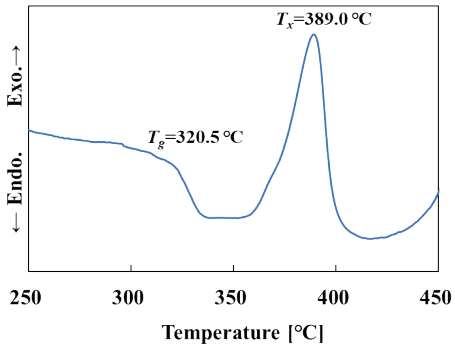

Fig. 3. (Color online) DTA profile of PG.

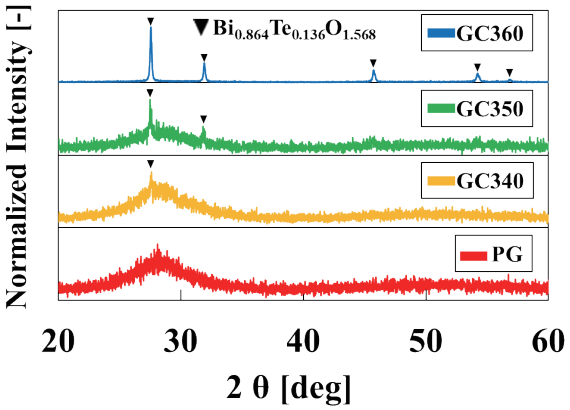

Fig. 4. (Color online) XRD patterns of PG, GC340, GC350, and GC360.

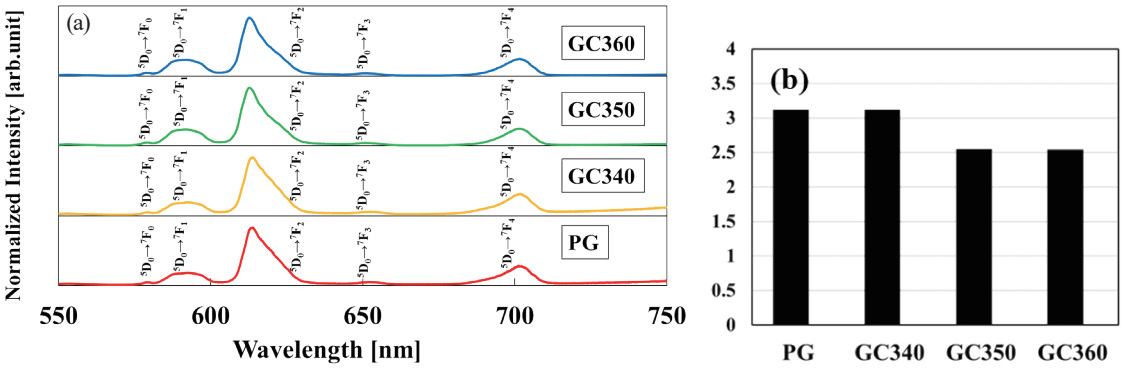

Fig. 5. (Color online) (a) PL spectra of PG, GC340, GC350, and GC360 at excitation wavelength of 530 nm. (b) R/O values.

Figure 6 shows the PL decay curves of PG, GC340, GC350, and GC360. Emissions were monitored at 610 nm under 530 nm excitation light. The observed decay times were 0.78 ms for PG, 0.78 ms for GC340, 0.78 ms for GC350, and 0.84 ms for GC360. These decay times were attributable to the transition between 4f levels in Eu^{3+}, and no significant change in lifetime was observed with increasing heat treatment temperature.[17–19]

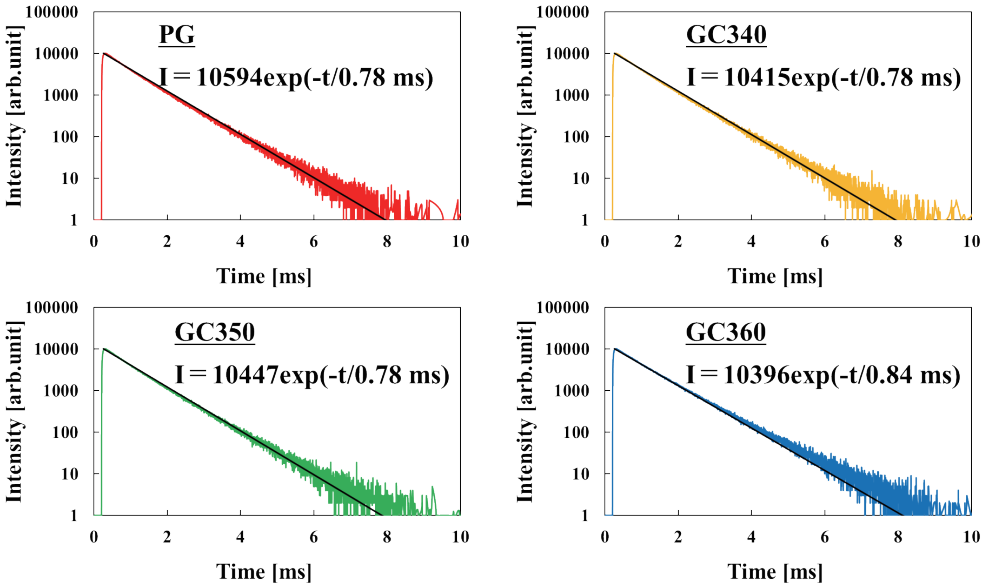

Fig. 6. (Color online) PL decay time profiles of PG, GC340, GC350, and GC360.

To investigate PL properties in detail, the radiative decay rate (k_f) of the $^5D_0 \rightarrow {}^7F_2$ transition and the nonradiative decay rate (k_{nr}) of the $^5D_0 \rightarrow {}^7F_2$ transition were derived using the *QY* and decay time of the $^5D_0 \rightarrow {}^7F_2$ transition shown in Table 2.[18,19]

$$QY = \frac{k_f}{k_f + k_{nr}} \tag{1}$$

$$\tau = \frac{1}{k_f + k_{nr}} \tag{2}$$

Table 2 lists the k_f and k_{nr} of the $^5D_0 \rightarrow {}^7F_2$ transition. A significant decrease in k_f owing to heat treatment was observed. On the other hand, k_{nr} was not changed drastically by heat treatment. The results indicate that the generation of the $Bi_{0.864}Te_{0.136}O_{1.568}$ crystalline phase was responsible for the decreases in k_f and *QY*. As mentioned earlier, the R/O ratio is related to the symmetry of the surrounding environment on Eu^{3+}, suggesting that the higher symmetry induced by the $Bi_{0.864}Te_{0.136}O_{1.568}$ crystalline phase should lead to the decrease in k_f. In the case of the emissions from Eu^{3+}, the Ω_2 of the Judd–Ofelt parameter is associated with the R/O ratio ($I_{R/O}$).[19,23]

$$\Omega_2 = \frac{D_{MD}\lambda_2^3}{e^2\lambda_1^3} \frac{9n^3 I_{R/O}}{n\left(n^2+2\right)^2 \left|\Psi J\right| \left|U^i\right| \left|\Psi' J'\right|^2} \tag{3}$$

Here, $|\Psi J||U^i||\Psi' J'|^2$ is the doubly reduced matrix element of the unit tensor operator, D_{MD} is the magnetic dipole transition strength, λ_1 ($^5D_0 \rightarrow {}^7F_1$) and λ_2 ($^5D_0 \rightarrow {}^7F_2$) are the luminescence

Table 2
Physical parameters of PG, GC340, GC350, and GC360.

	PG	GC340	GC350	GC360
Radiative decay rate of the $^5D_0 \rightarrow {}^7F_2$ transition (10^2 s^{-1})	14.1	13.5	7.76	8.27
Nonradiative decay rate of the $^5D_0 \rightarrow {}^7F_2$ transition (10^3 s^{-1})	1.14	1.15	1.20	1.11
PL decay time (ms)	0.78	0.78	0.78	0.84
QY of the $^5D_0 \rightarrow {}^7F_2$ transition (%)	11	11	6.1	6.9

wavelengths, *e* is the electron charge, and *n* is the refractive index. On the assumption that the *n* values of PG, GC340, GC350, and GC360 were almost the same based on the previous values obtained for tellurite glass and glass ceramics,[19] Ω_2 could have a positive correlation with the R/O ratio ($I_{R/O}$); therefore, k_f and *QY* decreased after the heat treatment since a low Ω_2 should lead to a low radiative decay rate for the $^5D_0 \rightarrow {}^7F_2$ transition.[19,23]

To investigate the scintillation properties under X-ray irradiation, the scintillation spectra of PG, GC340, GC350, and GC360 were recorded (Fig. 7). Luminescence peaks appeared at 579, 590, 615, 654, and 703 nm. The observed spectral shapes were similar to those of PL (Fig. 5); thus, the emissions were also derived from the transitions between the 4f levels of Eu^{3+}.[21–23] Furthermore, Table 3 lists the relative ratios of the integrated scintillation intensities of PG, GC340, GC350, and GC360 to that of the $Bi_4Ge_3O_{12}$ scintillator. As shown in Table 3, the scintillation intensity increased with the heat treatment temperature of PG. The relative *QY*s and relative integrated scintillation intensities of PG, GC340, GC350, and GC360 are shown in Fig. 8. The highest *QY* was obtained from PG, whereas GC360 showed the highest integrated scintillation intensity. Scintillation intensity (*LI*) is expressed as follows.[1,26]

$$LI \propto \frac{E_r}{\beta E_g} \times S \times QY \tag{4}$$

Here, E_r is the energy of radiation, E_g is the band gap energy, β is a constant, and *S* is the energy transfer efficiency. *QY* was decreased by the precipitation of the $Bi_{0.864}Te_{0.136}O_{1.568}$ crystalline phase, but the scintillation intensity was increased (Fig. 8), suggesting an improvement in energy transfer efficiency. This might be because the number of quenching centers (e.g., nonbridged oxygen) in the glass material was reduced by heat treatment. The precipitation of the crystalline phase could lead to a decrease in the number of quenching centers. Furthermore, because of the heat treatment, the number of quenching centers might also decrease in the glass phase since the scintillation light yield of Ce-doped silicate glasses changed owing to their different thermal histories.[7]

Furthermore, the scintillation decay curves of PG, GC340, GC350, and GC360 were also measured (Fig. 9). The scintillation decay time profile consists of two exponential decay functions. The first component was considered to originate from the instrument response. The lifetimes of the second component for PG, GC340, GC350, and GC360 were all about 0.6 ms, and the second component originated from the transition between 4f levels in Eu^{3+}.[17,18] The obtained scintillation values were close to PL values.

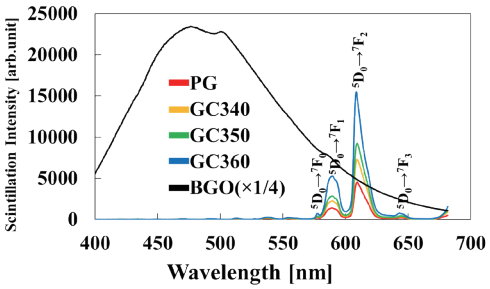

Fig. 7. (Color online) Scintillation spectra of PG, GC340, GC350, and GC360 under X-ray irradiation.

Table 3
Physical parameters of PG, GC340, GC350, and GC360.

	PG	GC340	GC350	GC360
Radiative decay rate of the $^5D_0 \rightarrow {}^7F_2$ transition (10^2 s^{-1})	14.1	13.5	7.76	8.27
Nonradiative decay rate of the $^5D_0 \rightarrow {}^7F_2$ transition (10_3 s^{-1})	1.14	1.15	1.20	1.11
PL decay time (ms)	0.78	0.78	0.78	0.84
QY of the $^5D_0 \rightarrow {}^7F_2$ transition (%)	11	11	6.1	6.9

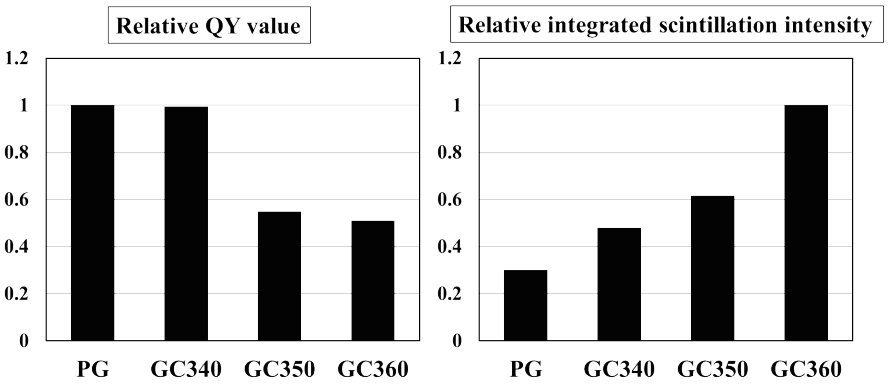

Fig. 8. (Color online) Relative *QY*s under 530 nm excitation light and relative scintillation intensities under X-ray irradiation.

In addition, the afterglow profiles of PG, GC340, GC350, and GC360 were recorded (Fig. 10). The afterglow level (AGL) was obtained from previous work using the signal intensity 20 ms after X-ray irradiation was stopped.[22] The AGLs were 198 ppm for PG, 185 ppm for GC340, 183 ppm for GC350, and 162 ppm for GC360. These AGLs were lower than the AGL of CsI(Tl) (about 300 ppm measured with the same setup).[27] Moreover, it was found that the AGL decreased with increasing heat treatment temperature. Afterglow is a phenomenon associated with storage luminescence stimulated by thermal energy at room temperature and should be related to the number of shallow trapping centers; therefore, heat treatment might lead to a decrease in the number of shallow traps. The decrease in the AGL was consistent with the suggestion of a possible increase in energy transfer efficiency.[18]

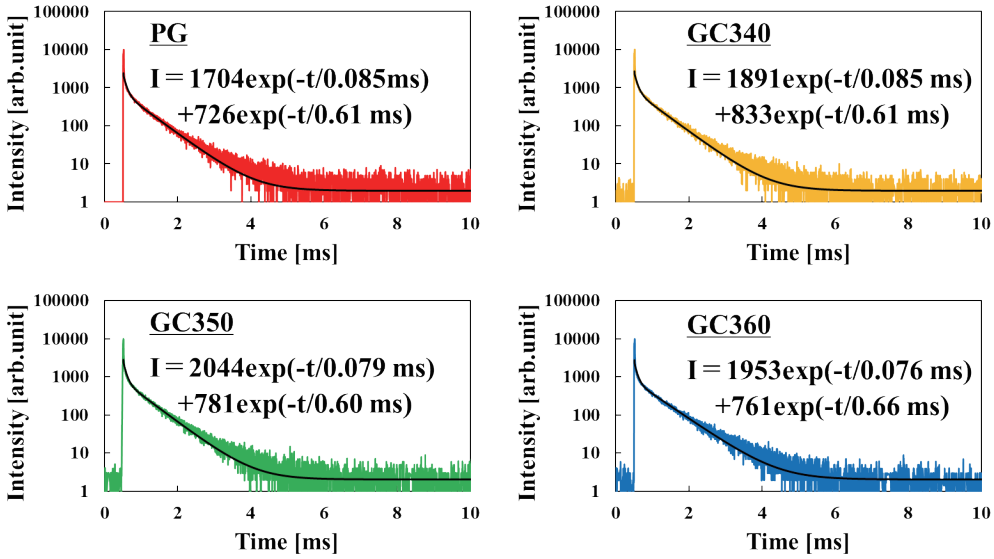

Fig. 9. (Color online) Scintillation decay curves of PG, GC340, GC350, and GC360.

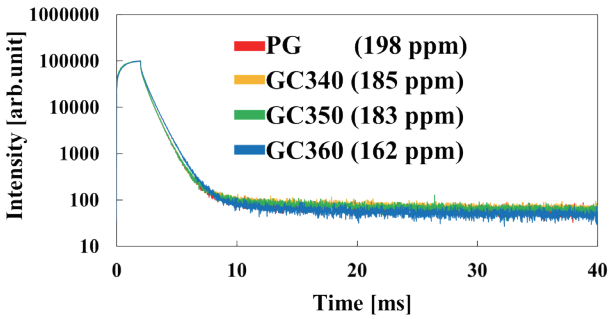

Fig. 10. (Color online) Afterglow profiles of PG, GC340, GC350, and GC360.

4. Conclusions

Tellurite glass (PG) with the composition of $1Eu_2O_3$–$13Bi_2O_3$–$12ZnO$–$74TeO_2$ and its glass ceramics (GC340, GC350, and GC360) were prepared. Clear luminescence peaks attributable to the transition between 4f levels in Eu^{3+} appeared in PG, GC340, GC350, and GC360. The obtained *QY* of PL was decreased by glass crystallization. On the other hand, the scintillation intensity was improved by heat treatment, and the scintillation intensity of GC360 was about three times that of PG, suggesting the improvement in energy transfer efficiency by the heat treatment.

Acknowledgments

This work was supported by a Grant-in-Aid B (24K03197) from the Japan Society for the Promotion of Science.

References

1 T. Yanagida: Proc. Jpn. Acad. Ser. B. Phys. Biol. Sci. **94** (2018) 75. https://doi.org/10.2183/pjab.94.007
2 P. Lecoq: Nucl. Instrum. Methods Phys. Res. A **809** (2016) 130. https://doi.org/10.1016/j.nima.2015.08.041
3 H. Takahashi, N. Hirade, N. Uchida, K. Hirose, T. Mizuno, Y. Fukazawa, K. Yamaoka, H. Tajima, and M. Ohno: Nucl. Instrum. Methods Phys. Res. A. **989** (2021) 164945. https://doi.org/10.1016/j.nima.2020.164945
4 W. J. Huang, Y. Li, J. Y. Chen, Y. F. Zhao, L. P. Chen, and H. Guo: Ceram. Int. **49** (2023) 8863. https://doi.org/10.1016/j.ceramint.2022.11.042
5 P. Boontueng, N. Ritjoho, N. Wantana, P. Limkitjaroenporn, H. Kim, T. Sanghangthum, N. Chanlek, A. Limphirat, Y. Yan, and J. Kaewkhao: Radiat. Meas. **163** (2023) 106937. https://doi.org/10.1016/j.radmeas.2023.106937
6 K. Miyazaki, D. Nakauchi, T. Kato, N. Kawaguchi, and T. Yanagida: Opt. Mater. **146** (2023) 114557. https://doi.org/10.1016/j.optmat.2023.114557
7 M. Bliss, R. A. Craig, and P. L. Reeder: Nucl. Instrum. Methods Phys. Res. A **342** (1994) 357. https://doi.org/10.1016/0168-9002(94)90263-1
8 W. Dai, Q. Zhang, G. A. Ashraf, H. Gong, R. Wei, H. Guo, and F. Hu: Ceram. Int. **50** (2024) 21878. https://doi.org/10.1016/j.ceramint.2024.03.301
9 H. Masai, G. Okada, N. Kawaguchi, and T. Yanagida: J. Non-Cryst. Solids. **501** (2018) 131. https://doi.org/10.1016/j.jnoncrysol.2017.11.026
10 J. Tang, Z. Lin, D. Tu, T. Wei, R. Duan, and S. Zhou: J. Non-Cryst. Solids. **15** (2022) 100110. https://doi.org/10.1016/j.nocx.2022.100110
11 L. Huang, S. Jia, Y. Li, S. Zhao, D. Deng, H. Wang, G. Jia, Y. Hua, and S. Xu: Nucl. Instrum. Methods Phys. Res. A. **788** (2015) 111. https://doi.org/10.1016/j.nima.2015.03.084
12 J. T. Zhao, L. H. Huang, S. L. Zhao, and S. Q. Xu: Opt. Mater. Express. **9** (2019) 576. https://doi.org/10.1364/OME.9.000576
13 C. B. Deng, M. Z. hang, T. Lan, M. J. Zhou, Y. Wen, J. Zhong, and X. Y. Sun: J. Non-Cryst. Solids. **554** (2021) 120565. https://doi.org/10.1016/j.jnoncrysol.2020.120565
14 A. Takaku, N. Kawano, H. Kimura, D. Nakauchi, M. Akatsuka, K. Shinozaki, and T. Yanagida: Jpn. J. Appl. Phys. **61** (2022) 1034. https://doi.org/10.35848/1347-4065/ac1f65
15 R. Nakamori, N. Kawano, A. Takaku, D. Onoda, Y. Takebuchi, H. Fukushima, T. Kato, K. Shinozaki, and T. Yanagida: Sens. Mater. **34** (2022) 707. https://doi.org/10.18494/sam3689
16 N. Kawano, K. Okazaki, Y. Takebuchi, H. Fukushima, T. Kato, D. Nakauchi, F. Kagaya, K. Shinozaki, and T. Yanagida: Jpn. J. Appl. Phys. **62** (2023) 072002. https://doi.org/10.35848/1347-4065/ace013
17 R. Nakamori, N. Kawano, A. Takaku, D. Nakauchi, H. Kimura, M. Akatsuka, K. Shinozaki, and T. Yanagida: Mater. Res. Bull. **145** (2022) 111547. https://doi.org/10.1016/j.materresbull.2021.111547
18 R. Nakamori, N. Kawano, D. Nakauchi, T. Kato, H. Fukushima, Y. Takebuchi, K. Shinozaki, and T. Yanagida: J. Mater. Sci. Mater. Electron. **33** (2022) 20470. https://doi.org/10.1007/s10854-022-08861-y
19 R. Nakamori, N. Kawano, D. Nakauchi, T. Kato, D. Shiratori, H. Fukushima, Y. Takebuchi, K. Shinozaki, and T. Yanagida: Ceram. Int. **49** (2023) 15884. https://doi.org/10.1016/j.ceramint.2023.01.183
20 X. Hu, G. Guery, J. Boerstler, J. D. Musgraves, D. Vanderveer, P. Wachtel, and K. Richardson: J. Non-Cryst. Solids. **358** (2012) 952. https://doi.org/10.1016/j.jnoncrysol.2012.01.009
21 T. Yangida, K. Kamada, Y Fujimoto, H. Yagi, and T. Yanagidani: Opt. Mater. **35** (2013) 2480. https://doi.org/10.1016/j.optmat.2013.07.002
22 T. Yanagida, Y. Fujimoto, T. Ito, K. Uchiyama, and K. Mori: Appl. Phys. Express **7** (2014) 062401. https://doi.org/10.7567/APEX.7.062401
23 A. Ciric, S. Stojadinovic, M, Sekulic, and M. D. Dramicanin: J. Lumin. **205** (2019) 351. https://doi.org/10.1016/j.jnoncrysol.2011.06.032
24 A. X. Hu, G. Guery, J. D. Musgraves, D. VanDerveer, J. Boerstler, N. Carlie, P. Wachtel, S. Raffy, R. Stolen, and K. Richardson: J. Non-Cryst. Solids. **357** (2011) 3648. https://doi.org/10.1016/j.jnoncrysol.2011.06.032
25 X. Zhang, Y. Fu, Z. Zhao, J. Yang, N. Li, and M. Zhang: J. Lumin. **194** (2018) 311. https://doi.org/10.1016/j.jlumin.2017.09.058
26 D. J. Robbins: J. Electrochem. Soc. **127** (1980) 2694. https://doi.org/10.1149/1.2129574
27 S. Takase, K. Miyazaki, D. Nakauchi, T. Kato, N. Kawaguchi, and T. Yanagida: J. Lumin. **267** (2024) 120400. https://doi.org/10.1016/j.jlumin.2023.120400